Defining the Nanostructured Morphology of Triblock Copolymers Using Resonant Soft X-ray Scattering

8 AUTHORS, INCLUDING:

Dong Hyun Lee
Asan Medical Center
327 PUBLICATIONS **3,573** CITATIONS

SEE PROFILE

Alexander Hexemer
University of California, Berkeley
90 PUBLICATIONS **1,954** CITATIONS

SEE PROFILE

Hirokazu Hasegawa
Kyoto University
163 PUBLICATIONS **4,894** CITATIONS

SEE PROFILE

Harald Werner Ade
North Carolina State University
355 PUBLICATIONS **8,628** CITATIONS

SEE PROFILE

Defining the Nanostructured Morphology of Triblock Copolymers Using Resonant Soft X-ray Scattering

Cheng Wang,[*,†,∇] Dong Hyun Lee,[‡,∇] Alexander Hexemer,[†] Myung Im Kim,[§] Wei Zhao,[∥] Hirokazu Hasegawa,[⊥] Harald Ade,[#] and Thomas P. Russell[*,∥]

[†]Advanced Light Source, Lawrence Berkeley National Laboratory, Berkeley, California 94720, United States

[‡]Department of Polymer Science and Engineering, Dankook University, 126, Jukjeon-dong, Suji-gu, Yongin-si, Gyeonggi-do, 448-701, Korea

[§]College of Chemistry and Department of Materials Science and Engineering, University of California, Berkeley, California 94720-14604, United States

[∥]Department of Polymer Science and Engineering, University of Massachusetts, Amherst, Massachusetts 01003, United States

[⊥]Department of Polymer Chemistry, Graduate School of Engineering, Kyoto University, Japan

[#]Department of Physics, North Carolina State University, Raleigh, North Carolina 27650, United States

S Supporting Information

ABSTRACT: The morphologies of a poly(1,4-isoprene)-*block*-polystyrene-*block*-poly(2-vinyl pyridine) (IS2VP) copolymer were investigated using resonant soft X-ray scattering (RSoXS) together with scanning force microscopy, small-angle X-ray scattering, and electron microscopy. Differences in the nanoscopic morphologies in the bulk and thin film samples were observed arising from the competition between segmental interactions between the blocks and the substrate and the surface energies of each block. Using soft X-rays at selected photon energies to isolate the scattering contribution from different polymer blocks, RSoXS

unambiguously defined the complex morphology of the triblock copolymer. In the bulk sample, two nested, hexagonal arrays of P2VP and PI cylindrical microdomains residing in the PS matrix were observed. The cylindrical microdomains of one component were found to be located at the interstitial sites of the hexagonal array of the other component that has the larger *d* spacing. In solvent-annealed thin films with 40 nm in thickness, a hexagonal array of core−shell microdomains of P2VP cores with PS shells that reside in a PI matrix were observed.

KEYWORDS: Block copolymer, ABC triblock copolymer, core−shell, soft X-ray scattering, RSoXS, electron tomography
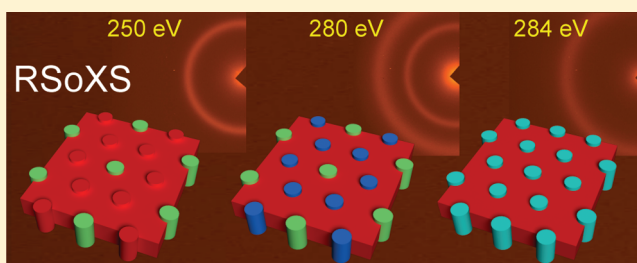
Block copolymers (BCPs), chemically distinct polymers covalently joined together at the end(s) of the chains, can self-assemble into periodic arrays of microdomains, tens of nanometers in size, including lamellae (LAM), hexagonally packed cylinders (HEX), body-centered cubic packed spheres (BCC), and bicontinuous gyroids (Ia3d) in bulk and in thin films. By selective removal of the components, sequential chemistries within the different microdomains, or a combination of these two, BCPs can be used as templates and scaffolds for the design and fabrication of compound nanoscopic structures and devices.[1−6] While there have been extensive studies on AB-type diblock copolymers, there have been fewer studies on ABC-type triblock copolymers, due to the more demanding synthesis involved and the complexity of the morphologies. However, as discussed by others,[7−12] the addition of a third block results in a wealth of periodic morphologies. Yet, to fully realize the potential of these materials, it is essential to understand their morphologies and the parameters that control the orientation and ordering of these molecules.

With AB-type diblock copolymers, the segmental interaction parameter (χ) and volume fractions (f) of the components define the nature of their morpholology. The total molecular weight of the copolymer chain (N) will dictate the overall size.[7,8,13,14] By contrast, in the absence of an applied external field, interfacial and surface energies will govern the morphology and orientation in thin films. However, in the case of ABC-type triblock copolymer, the sequencing of three chemically different components in copolymer, the order of blocks along a chain, should be considered to account for the variety of their unique morphologies with the existing factors mentioned above. There are several notable studies on the morphologies of ABC-type triblock copolymers.[9,10,15−24] Stadler and co-workers pioneered studies on these types of block copolymers.[9,10] They uncovered an abundance of nanostructures arisen from ABC-type triblock copolymers
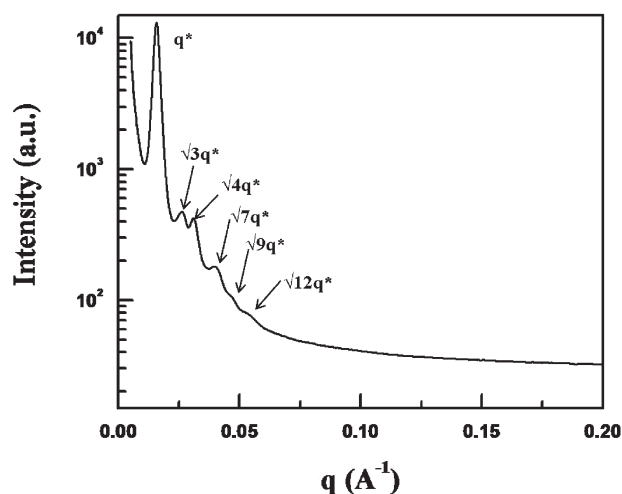
Figure 1. SAXS profile of poly(1,4-isoprene)-*block*-polystyrene-*block*-poly(2-vinyl pyridine) copolymer.
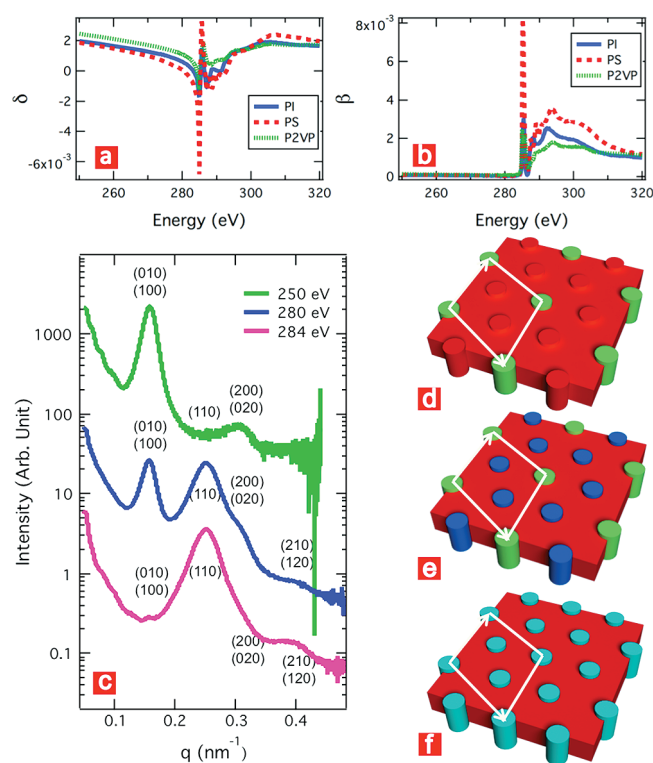

Figure 2. (a, b) Real (δ) and imaginary (β) part of the complex index of refraction of poly(1,4-isoprene) (blue solid line), polystyrene (red dashed line), and poly(2-vinyl pyridine) (green dotted line), respectively. (c) 1D plot of radial averaged scattering intensity vs q at 250, 280, and 284 eV, from top to bottom respectively. (d–f) Schematic illustration of hexagonally packed cylindrical morphology of IS2VP triblock copolymer seen by X-rays at different energies.

such as polystyrene-*block*-polybutadiene-*block*-poly(methyl methacrylate) and polystyrene-*block*-poly(ethylene-*co*-butylene)-*block*-poly(methyl methacrylate) copolymers. Bates and co-workers reported various nanostructures that polystyrene-*block*-polyisoprene-*block*-poly(ethylene oxide) triblock copolymers form, including multilayered lamellae, core–shell cylinders, and

core–shell gyroids.[15,16,20] Mastushita and co-workers reported that polyisoprene-*block*-polystyrene-*block*-poly(2-vinyl pyridine) (IS2VP) and polystyrene-*block*-polyisoprene-*block*-poly(2-vinyl pyridine) (SI2VP) copolymers exhibited other unique morphologies, e.g., four-layer lamellae, ordered tricontinuous double diamonds (OTDD), by adjusting the volume fraction of the middle block in ABC triblock copolymers.[21–23] However, thorough characterization and understanding of multiblock copolymer are relegated to only a few studies and a comprehensive understanding has yet to emerge.

In this paper, we present the morphologies of a poly(1, 4-isoprene)-*block*-polystyrene-*block*-poly(2-vinyl pyridine) based triblock copolymer (IS2VP) in the bulk and in thin films as determined by resonant soft X-ray scattering (RSoXS),[25–31] scanning force microscopy (SFM), transmission electron microscopy (TEM), small-angle X-ray scattering (SAXS), and grazing incident small-angle X-ray scattering (GISAXS). RSoXS unambiguously revealed the coassembly of two nested hexagonally packed arrays in the bulk and the core–shell structure in the thin films, complementing other key insights provided by electron tomography and hard X-ray scattering.

Figure 1 shows the radial avaraged SAXS profile of an IS2VP triblock copolymer bulk sample. SAXS data were acquired at Beamline 7.3.3, Advanced Light Source (ALS).[32] Since the first-order and higher order scattering peaks can be assigned as q^*, $\sqrt{3}q^*$, $\sqrt{4}q^*$, $\sqrt{7}q^*$, $\sqrt{9}q^*$, and $\sqrt{12}q^*$ as shown in Figure 1, the SAXS data show that the overall morphology consists of hexagonally packed cylindrical microdomains. Even though hexagonal arrays of cylindrical microdomains are observed in hard X-ray scattering experiments as exhibited in Figure 1, the spatial arrangement of PI and P2VP microdomains in PS matrix still remains unresolved if the composition of each block in IS2VP is considered. From the position of the first-order peak the d-spacing of the cylindrical microdomains is ~39 nm.

Panels a and b of Figure 2 show the real (δ) and imaginary part (β) of the complex index of refraction of PS, PI, and P2VP. δ was calculated through Kramer–Kronigs equation based on the absorption coefficient, β, which was obtained from the existing NEXAFS database.[33] Since the complex index of refraction is proportional to the X-ray scattering power of the materials, several photon energies across the carbon 1s absorption edge was selected with the goal of isolating the scattering contribution of different polymers. RSoXS data were taken at ALS beamline 11.0.1.2.[34] As shown in Figure 2c, the radially averaged RSoXS data of the IS2VP triBCP bulk sample showed significant differences between data acquired at various energies (250, 280, and 284 eV), as well as marked differences to the SAXS shown in Figure 1. At 280 eV, three scattering peaks were observed at 0.16, 0.27, and 0.32 nm^{-1}, respectively. These can be assigned to the primary reflection at q^*, $\sqrt{3}q^*$, and $\sqrt{4}q^*$ characteristic of a hexagonally packed structure. At 250 and 284 eV, the scattering patterns look dramatically different, with one strong scattering peak observed at both energies. Significantly, the corresponding scattering vectors were very different: 0.16 nm^{-1} for 250 eV and 0.27 nm^{-1} for 284 eV. This observation indicates that two completely different lattices were observed at these two energies. As shown in panels a and b of Figure 2, below the carbon 1s absorption edge, the absorptions, β, of all three polymers are close to zero. Therefore, the contrasts between different components are mainly lying in the differences in δ, the real part of the scattering power, at different photon energies. For example, at 250 eV, $\delta_{PS} \approx 0.0019$, $\delta_{P2VP} \approx 0.0024$, $\delta_{PI} \approx 0.0019$, the soft

X-ray scattering contrast between PS and PI is virtually zero, and "index-matching" between these two constituent components is achieved. Consequently, the lattice of the P2VP in the "PI-PS" matrix is detected. Conversely, at 284 eV, the contrast between P2VP and PI domains is minimized. At 280 eV, the index of refraction of all three polymers is different enough to yield significant contract between any two components.

At 250 eV, only the hexagonal lattice of P2VP is detected with a strong peak at $q^* \sim 0.16$ nm^{-1} and another small peak that corresponds to $\sim \sqrt{4}q^*$. The observed structure is illustrated in Figure 2d; the hexagonal unit cell is marked with white arrows. The unit cell is composed of P2VP cylinders that are located at $(0,0,0)$ position in crystallographic coordinates. The P2VP lattice constant $a = \sim45$ nm, which corresponds to the lattice spacing of ~39 nm for the hexagonal structure. In the kinematical approximation of the scattering, the scattering intensity $I(\mathbf{q})$ can be expressed as

$$I(\mathbf{q}) \propto |F(\mathbf{q})|^2$$

$F(\mathbf{q})$ is commonly referred as the structure factor

$$F(\mathbf{q}) = \sum_j f(\mathbf{q})_j e^{-i\mathbf{q}\cdot\mathbf{r}_j}$$

where $f(\mathbf{q})_j$ is the form factor (scattering power) of the polymer domain, and $\mathbf{r}_j$ is the jth domain position in the crystal coordinate. Because the scattering peak only occurs if the scattering vector $\mathbf{q}$ is equal to the reciprocal lattice vector, the structure factor can be expressed with Miller indices (hkl), $F(hkl)$. At 250 eV, the refraction indices of PS and PI are matched, so there will not be scattering from the PI/PS interface, only P2VP domains are contributed to the scattering. Therefore

$$F(hkl) = f(\mathbf{q})_{P2VP}$$

the q^* scattering peak should correspond to the (100) and (010) reflection, the $\sqrt{3}q^*$ peak should correspond to the (110) reflection, and $\sqrt{4}q^*$ correspond to the (200) and (020) reflection. In this case the intensity of the scattering peaks is mainly based on the q-dependent form factor of the P2VP domain and on how well the domains are ordered. The (100) and (010) reflection at q^* of ~0.16 nm is readily observed in the 250 eV data as well as the third-order peak corresponding to the (200) plane. However, the expected reflection at the (110) plane which is $\sqrt{3}q^*$ is not observed. This is because the scattering form factor of the P2VP cylindrical microdomains has a node at this q value that overlaps with $\sqrt{3}q^*$. From a simple simulation of the cylindrical form factor,[35] the diameter of the P2VP cylinder can be determined to be ~26 nm. (Figure S5, Supporting Information).

At 280 eV, as shown in Figure 2d, the contrasts between all the polymers are significant, both P2VP and PI domains are visible and the unit cell of the hexagonal lattice is now composed of a P2VP cylinder at $(0,0,0)$ and two PI cylinders at $(1/3, 2/3, 0)$ and $(2/3, 1/3, 0)$, respectively. The structure factors for different (hkl) planes are now

$$F(100) = F(010) = f(\mathbf{q})_{P2VP} - f(\mathbf{q})_{PI}$$

$$F(110) = f(\mathbf{q})_{P2VP} + 2f(\mathbf{q})_{PI}$$

$$F(200) = F(020) = f(\mathbf{q})_{P2VP} - f(\mathbf{q})_{PI}$$

Scattering peaks corresponding to all planes are well pronounced, especially the peak at the (110) position, which is
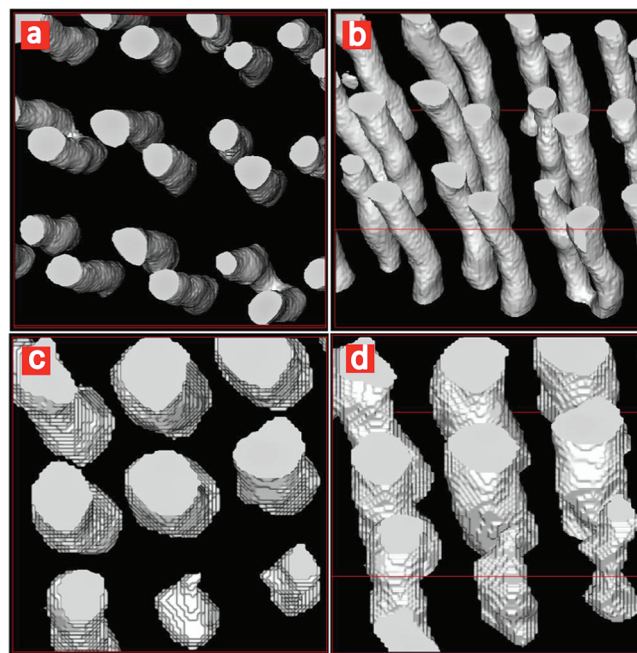

Figure 3. 3D electron tomography (TEMT) images of poly(1,4-isoprene)-*block*-polystyrene-*block*-poly(2-vinyl pyridine) copolymer: (a, b) stained with osmium tetraoxide vapor; (c, d) stained with 1,4-di-iodobutane, respectively. (b) and (d) are obtained by tilting (a) and (c), respectively. (a) and (b) are presenting PI cylinders stained by OsO4 while (c) and (d) are presenting P2VP cylinders stained by 1,4-di-iodobutene. The volume sizes of the reconstructed images of PI microdomains and P2VP microdomains are $67 \times 67 \times 30$ nm^3 and $53 \times 53 \times 21$ nm^3, respectively.

much more intense compared to the 250 eV data (Figure 2c). This is mainly due to the scattering contribution from PI domains, as the P2VP scattering form factor has a node, $f(\mathbf{q})_{P2VP} \rightarrow 0$, at this q value.

At 284 eV, the contrast between PI and P2VP domains is minimal; the scattering powers of the PI and P2VP are similar, therefore

$$f(\mathbf{q})_{P2VP} = f(\mathbf{q})_{PI}$$

and

$$F(100) = F(010) = 0$$

$$F(110) = f(\mathbf{q})_{P2VP} + 2f(\mathbf{q})_{PI}$$

$$F(200) = F(020) = 0$$

The scattering intensity for the (100), and (010) reflections becomes zero as along with the (200) and (020) reflections. As a result, scattering peaks at 0.16 and 0.32 nm^{-1} disappear and a strong reflection at ~0.27 nm^{-1} is present that corresponds to the (110) plane with a d spacing of ~23 nm. At this energy, the scattering corresponds to the scattering from a hexagonal cylindrical structure with a smaller lattice constant ($\sqrt{3}/3$ of the P2VP lattice).

At 280 eV, there is contrast for both P2VP and PI and, as such, interference and superposition arising from the spatial distribution of both microdomains are evident. These results are consistent with the electron tomography results presented in

Figure 3. It clearly indicates that the PI and P2VP microdomains formed, at least locally, independent cylindrical microdomains in a PS matrix. A summary of these conclusions are shown schematically in Figure 2e where the green domain represents P2VP, the blue represents PI, and the red represents the PS. This morphology is consistent with the triblock architecture: the middle block forms the matrix and each end forms its own cylindrical domain on a hexagonal lattice. A different perspective and description to define this uncommon structure is that the bulk system is forming a closed pack hexagonal core—shell structure with the P2VP core and PS shell in a PI matrix. However, the diameter of the core—shell is matching the distance between two core—shells, and the PI located at the corner is pushed to form a stand-alone cylinder, which gives rise to a new phase composed of nested hexagonal cylinders.

The primary scattering peaks corresponding to (010) and (100) reflections observed at 250 and 280 eV were suppressed at 284 eV. This corresponds to the dominant lattice spacing of ~39 nm observed with SAXS. The relative contrast between PS, P2VP, and PI polymers in the hard X-ray regime allows different orders of scattering peaks to be observed. Interestingly, the RSoXS data taken at 260 eV show almost the same relative scattering peak intensity in comparison to the SAXS data (Figure S4, Supporting Information). On the basis of comparable carbon/hydrogen ratios and densities, the electron density difference between these two materials for hard X-ray scattering is small. Furthermore, since the scattering peak corresponding to the smaller lattice due to the PI domains is observed at $\sqrt{3}/3$ of the P2VP lattice, distinguishing the contributions from different polymer domains is difficult with hard X-rays. Consequently, it is impossible to discern the correct morphology using only hard X-rays.

3D transmission electron microscopy tomography (TEMT) was used to independently assess the local structure of the IS2VP triblock copolymer employed in this study. TEMT, on microtomed samples, provides a three-dimensional image by reconstructing the images obtained at different tilt angles of the sample with respect to the incident electron beam. The software IMOD was used for reconstruction and Analyze 9.0 was used for visualization into 3D images.[36,37] Panels a and b of Figure 3 exhibit such reconstructed images of osmium tetraoxide (OsO_4) stained PI microdomains. Here, the cylindrical nature of the PI microdomains array is clearly evident. Panels c and d of Figure 3 show reconstructed images of the 1,4-diiodobutane stained P2VP microdomains. Again, cylindrical microdomains are evident. There is no evidence of a network morphology that has been reported by others.[9,10,15−24] Consequently, the TEMT results are fully consistent with the RSoXS results where the morphology consists of two arrays of cylindrical microdomains embedded within each other, with the PI microdomains located at the interstitial sites of the larger P2VP hexagonal lattice.

The field of view of the TEMT results shown in Figure 3 is too small to clearly show a hexagonal lattice from the IS2VP triblock copolymer. This is more clearly observed by regular TEM as shown in the Figure S3 (Supporting Information). How dominant the interpenetrating hexagonal lattice morphology is throughout the whole sample is best assessed with the scattering results shown in Figures 1 and 2, as RSoXS and SAXS are methods that average over much larger sample areas and thicker samples than TEMT and TEM. Overall, the scattering data indicate that the hexagonal structures are well developed throughout the sample.
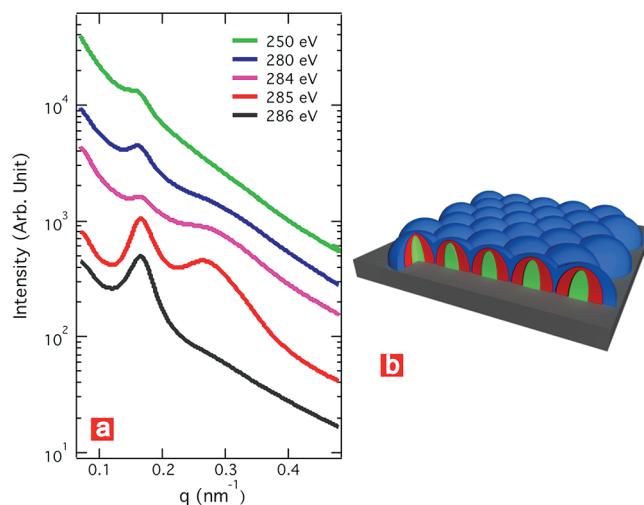

Figure 4. (a) RSoXS data of thin film poly(1,4-isoprene)-*block*-polystyrene-*block*-poly(2-vinlypyridine). Radial averaged scattering intensity vs q plot of 250, 280, 284, 285, and 286 eV, from top to bottom, respectively. (b) Schematic illustration of core—shell structure of the IS2VP thin film.

In contrast to the bulk samples discussed above, the morphologies observed in the solvent-annealed thin films were different. Grazing incidence X-ray scattering (GISAXS) and scanning force microscopy (SFM) (Figures S1 and S2, Supporting Information) showed well-defined hexagonally packed nanostructures with an average diameter of 36.8 nm and a center-to-center distance of 45 nm. SFM probes only the surface of the films, while the contrast provided by hard X-rays, as discussed above, is not optimal to assess the finer details of the morphology of IS2VP. The enhanced scattering cross section provided by RSoXS provides sufficient scattering intensity for polymer films only ~40 nm thick to study them in transmission.[26,27] It is noted that for scattering of thin films in transmission geometry, the observed structure is averaged over the film thickness. Further investigations using grazing incidence soft X-ray scattering that will aid in quantifying the depth profile of the thin film are in progress. RSoXS results for triBCP thin films acquired at the X-ray energies as noted are shown in Figure 4. There is a distinct dependence of the scattering on the energy of the incident X-rays that provides detailed information on the morphology formed in the thin films. The radial averaged scattering intensities of these data sets are plotted in Figure 4a. At 250 eV, where the PI and PS optical properties are matched, one scattering maximum is observed at $q^* \sim 0.16$ nm^{-1}. This corresponds to a spacing of ~39 nm, which can be attributed to the (010) and (100) lattice plane of P2VP microdomains oriented normal to the film surface. No higher order reflections were observed at this energy. At 280 eV, the same (010) reflection is clearly evident with an increase in intensity at the higher q values. At 284 eV, the scattering at higher q values is very significant and broad reflections corresponding to $\sqrt{3}q^*$, and $\sqrt{4}q^*$ of the hexagonal lattice are seen. At 285 eV, the relative intensities between the q^* peak and the $\sqrt{3}q^*$ and $2q^*$ peaks are rather different than in the data obtained at 284 eV. At 286 eV only the very intense first peak (q^*) is observed. The same q^* is seen for all X-ray energies, while variations in peak intensity for the higher order reflections are evident. Since the same low q^* peak is observed at all energies, the basic center-to-center distance for all polymer components is

the same and these variations must correspond to a core—shell type of morphology instead of the nested hexagonal morphology observed in the bulk sample. If the contrast between the shell and matrix is negligible, only the core will be seen and the form factor will be that of the core. If there is no contrast between the core and the shell, the form factor will correspond to that of a combined core—shell. Only when there is contrast between the core, shell, and matrix will the form factor directly contain the information about the core—shell structure. For 250 and 286 eV, there is very little contrast between the PI and PS block. Furthermore, the form factor at these energies suppresses the $\sqrt{3}q^*$ and $\sqrt{4}q^*$ peaks. This must correspond to a small structure and at the same time must be the P2VP. We conclude therefore that the core is the P2VP block. For 280, 284, and 285 eV, the $\sqrt{3}q^*$ and $\sqrt{4}q^*$ peaks are clearly visible. At the same time the contrast between the PI and PS blocks are large enough to show the core—shell form factor. On the basis of the SFM, RSoXS results, the deduced core—shell structure is illustrated in Figure 4b. It is consistent with a previous inference of the morphology in these films.[1] The difference observed between the bulk and thin film morphologies arises from the preferential interactions of the components with the substrate and air interfaces. In thin films, this preferential segregation can effectively give rise to an apparent change in the volume fraction and induce a change in the morphologies. If the free energies of the morphologies are not that different, then subtle changes in the volume fractions of the component can affect a change in morphology. It should also be kept in mind that the preferential interactions will, also, cause a preferential orientation of the morphology in the thin film and, if the orientation is not complete or if it results in a frustration of the morphology, the morphology in the thin film can be significantly different than that in the bulk.

We determined the bulk and thin film morphology of an IS2VP-based triblock copolymer by using RSoXS together with SFM, TEM, TEMT, and SAXS/GISAXS. Hard X-ray scattering techniques indicated that solvent-annealed IS2VP thin film consisted of hexagonally packed nanostructures having long-range lateral order. RSoXS showed that the nature of these nanostructures was core—shell microdomains with a central P2VP core and a PS shell. In addition, RSoXS and TEMT revealed a novel bulk morphology consisting of two nested, hexagonal arrays of P2VP and PI microdomains. The P2VP cylindrical microdomains were hexagonally packed on the larger of the two lattices and surrounded by six small cylindrical PI domains located at the interstitial sites of the P2VP lattice.

ASSOCIATED CONTENT

⑤ Supporting Information. Experimental procedures and additional information about SFM, TEM, SAXS/GISAXS, and RSoXS data and simulation. This material is available free of charge via the Internet at http://pubs.acs.org.

AUTHOR INFORMATION

Corresponding Author
*E-mail: cwang2@lbl.gov, russell@mail.pse.umass.edu.

Author Contributions
▽Authors contributed equally.

REFERENCES

(1) Lee, D. H.; Park, S.; Gu, W. Y.; Russell, T. P. *ACS Nano* **2011**, 5, 1207–1214.
(2) Magbitang, T.; Lee, V. Y.; Miller, R. D.; Toney, M. F.; Lin, Z. L.; Briber, R. M.; Kim, H. C.; Hedrick, J. L. *Adv. Mater.* **2005**, 17, 1031–+.
(3) Melde, B. J.; Burkett, S. L.; Xu, T.; Goldbach, J. T.; Russell, T. P. *Chem. Mater.* **2005**, 17, 4743–4749.
(4) Zalusky, A. S.; Olayo-Valles, R.; Wolf, J. H.; Hillmyer, M. A. *J. Am. Chem. Soc.* **2002**, 124, 12761–12773.
(5) Zhao, D. Y.; Feng, J. L.; Huo, Q. S.; Melosh, N.; Fredrickson, G. H.; Chmelka, B. F.; Stucky, G. D. *Science* **1998**, 279, 548–552.
(6) Chao, C. C.; Wang, T. C.; Ho, R. M.; Georgopanos, P.; Avgeropoulos, A.; Thomas, E. L. *ACS Nano* **2010**, 4, 2088–2094.
(7) Bates, F. S.; Fredrickson, G. H. *Annu. Rev. Phys. Chem.* **1990**, 41, 525–557.
(8) Bates, F. S.; Fredrickson, G. H. *Phys. Today* **1999**, 52, 32–38.
(9) Auschra, C.; Stadler, R. *Macromolecules* **1993**, 26, 2171–2174.
(10) Stadler, R.; Auschra, C.; Beckmann, J.; Krappe, U.; Voigtmartin, I.; Leibler, L. *Macromolecules* **1995**, 28, 3080–3097.
(11) Knoll, A.; Horvat, A.; Lyakhova, K. S.; Krausch, G.; Sevink, G. J. A.; Zvelindovsky, A. V.; Magerle, R. *Phys. Rev. Lett.* **2002**, 89, 035501.
(12) Rehse, N.; Knoll, A.; Konrad, M.; Magerle, R.; Krausch, G. *Phys. Rev. Lett.* **2001**, 87, 035505.
(13) Hamley, I. W. *The physics of block copolymers*; Oxford University Press: Oxford, 1998.
(14) Leibler, L. *Macromolecules* **1980**, 13, 1602–1617.
(15) Bailey, T. S.; Hardy, C. M.; Epps, T. H.; Bates, F. S. *Macromolecules* **2002**, 35, 7007–7017.
(16) Bailey, T. S.; Pham, H. D.; Bates, F. S. *Macromolecules* **2001**, 34, 6994–7008.
(17) Gido, S. P.; Schwark, D. W.; Thomas, E. L.; Goncalves, M. D. *Macromolecules* **1993**, 26, 2636–2640.
(18) Hasegawa, H.; Tanaka, H.; Yamasaki, K.; Hashimoto, T. *Macromolecules* **1987**, 20, 1651–1662.
(19) Ludwigs, S.; Boker, A.; Voronov, A.; Rehse, N.; Magerle, R.; Krausch, G. *Nat. Mater.* **2003**, 2, 744–747.
(20) Shefelbine, T. A.; Vigild, M. E.; Matsen, M. W.; Hajduk, D. A.; Hillmyer, M. A.; Cussler, E. L.; Bates, F. S. *J. Am. Chem. Soc.* **1999**, 121, 8457–8465.
(21) Mogi, Y.; Kotsuji, H.; Kaneko, Y.; Mori, K.; Matsushita, Y.; Noda, I. *Macromolecules* **1992**, 25, 5408–5411.
(22) Mogi, Y.; Mori, K.; Kotsuji, H.; Matsushita, Y.; Noda, I.; Han, C. C. *Macromolecules* **1993**, 26, 5169–5173.
(23) Mogi, Y.; Nomura, M.; Kotsuji, H.; Ohnishi, K.; Matsushita, Y.; Noda, I. *Macromolecules* **1994**, 27, 6755–6760.
(24) Thomas, E. L.; Anderson, D. M.; Henkee, C. S.; Hoffman, D. *Nature* **1988**, 334, 598–601.
(25) Araki, T.; Ade, H.; Stubbs, J. M.; Sundberg, D. C.; Mitchell, G. E.; Kortright, J. B.; Kilcoyne, A. L. D. *Appl. Phys. Lett.* **2006**, 89, 124106.
(26) Swaraj, S.; Wang, C.; Yan, H. P.; Watts, B.; Jan, L. N.; McNeill, C. R.; Ade, H. *Nano Lett.* **2010**, 10, 2863–2869.
(27) Virgili, J. M.; Tao, Y.; Kortright, J. B.; Balsara, N. P.; Segalman, R. A. *Macromolecules* **2007**, 40, 2092–2099.
(28) Wang, C.; Araki, T.; Ade, H. *Appl. Phys. Lett.* **2005**, 87, 214109.

(29) Wang, C.; Araki, T.; Watts, B.; Harton, S.; Koga, T.; Basu, S.; Ade, H. *J. Vac. Sci. Technol., A* **2007**, *25*, 575–586.

(30) Wang, C.; Garcia, A.; Yan, H.; Sohn, K. E.; Hexemer, A.; Nguyen, T.-Q.; Bazan, G. C.; Kramer, E. J.; Ade, H. *J. Am. Chem. Soc.* **2009**, *131*, 12538–12539.

(31) Yan, H. P.; Swaraj, S.; Wang, C.; Hwang, I.; Greenham, N. C.; Groves, C.; Ade, H.; McNeill, C. R. *Adv. Funct. Mater.* **2010**, *20*, 4329–4337.

(32) Hexemer, A.; Bras, W.; Glossinger, J.; Schaible, E.; Gann, E.; Kirian, R.; MacDowell, A.; Church, M.; Rude, B.; Padmore, H. *J. Phys.: Conf. Ser.* **2010**, *247*, 012007.

(33) Dhez, O.; Ade, H.; Urquhart, S. *J. Electron Spectrosc.* **2003**, *128*, 85–96.

(34) Wang, C.; Hexemer, A.; Nasiatka, J.; Chan, E. R.; Young, A. T.; Padmore, H. A.; Schlotter, W. F.; Luning, J.; Swaraj, S.; Watts, B.; Gann, E.; Yan, H.; Ade, H. *IOP Conf. Ser.: Mater. Sci. Eng.* **2010**, *14*, 012016.

(35) Forster, S.; Apostol, L.; Bras, W. *J. Appl. Crystallogr.* **2010**, *43*, 639–646.

(36) Frank, J. *Electron tomography: methods for three-dimensional visualization of structures in the cell*, 2nd ed.; Springer: New York, 2006.

(37) Yamauchi, K.; Takahashi, K.; Hasegawa, H.; Iatrou, H.; Hadjichristidis, N.; Kaneko, T.; Nishikawa, Y.; Jinnai, H.; Matsui, T.; Nishioka, H.; Shimizu, M.; Fukukawa, H. *Macromolecules* **2003**, *36*, 6962–6966.